

Optical selection rules for electron-hole pair excitation in 3D topological insulators

Hari P. Paudel and Michael N. Leuenberger *

*NanoScience Technology Center and Department of Physics,
12424 Research Parkway Suite 400, Orlando, Florida 32826, United States*

Experiments using ARPES, which is based on the photoelectric effect, have shown that the surface states in 3D topological insulators (TI) are helical. Here we consider Weyl interface fermions due to band inversion in narrow-bandgap semiconductors, such as $\text{Pb}_{1-x}\text{Sn}_x\text{Te}$ and $\text{Bi}_{1-x}\text{Sb}_x$. We determine the optical selection rules of electron-hole pair excitation by means of the solutions of the 3D Dirac equation. While electron-hole pairs in graphene are generated through intraband transitions, we show that in 3D TI they are generated through both intraband and interband transitions. For their analysis, we calculate explicitly the electric dipole matrix elements by means of bandstructure calculations for $\text{Pb}_{1-x}\text{Sn}_x\text{Te}$. While in graphene the pseudospin helicity operator is given by $\hat{h}_g = -(1/|p_\perp|) \boldsymbol{\sigma} \cdot \mathbf{p}$, we define the spin helicity operator in 3D TI as $\hat{h}_{\text{TI}} = -(1/|p_\perp|) (\boldsymbol{\sigma} \times \mathbf{p}) \cdot \hat{\mathbf{z}}$, where $\hat{\mathbf{z}}$ points perpendicular to the interface. Our results are crucial for future opto-electronic devices based on 3D TI.

KEYWORDS: topological insulator, electron-hole pair, selection rule.

The 3D topological insulator (TI) is a new state of matter with unusual properties that manifest themselves on the surface or at the interface of narrow band gap materials where topologically protected gapless (metallic) surface/interface states appear within the bulk insulating gap [1–5]. These surface/interface states are characterized by the linear excitation energy of massless Weyl fermions. Protected by time-reversal symmetry, the spins of the Kramers partners are locked at a right angle to their momenta due to spin-orbit coupling, making them robust against perturbation and scattering [1, 2, 6, 7]. This means the larger the spin-orbit coupling, the better is the protection.

TIs can be found in a subclass of narrow-gap semiconductors where the band gaps are smaller than the typical energy scale of relativistic corrections to the bandstructures. The 2D TI exhibiting the quantum spin Hall effect was experimentally observed in HgTe quantum wells [8], where the interface of the well lead to a sign change of the mass term in the 2D Dirac equation, thereby creating a pair of gapless helical edge states inside the bulk energy gap. The origin of this hallmark for both 2D and 3D TIs is the Rashba spin-orbit coupling [9]. Helical edge modes have also been reported in a heterostructures of InAs/GaSb [10]. Many materials have been proposed as 3D TIs [11]. Because of the presence of a single Dirac cone with fixed spin direction at the *surface*, the main feature of strong TIs [12, 13], the materials Bi_2Se_3 and Bi_2Te_3 are currently being widely studied [5, 14].

The heterostructures of compound semiconductors such as $\text{Bi}_{1-x}\text{Sb}_x$ and $\text{Pb}_{1-x}\text{Sn}_x\text{Te}$ exhibit a strong topological phase [7]. In $\text{Bi}_{1-x}\text{Sb}_x$, with increasing x the gap at the L point decreases and the L^+ and L^- bands cross at $x = 0.04$. After further increase in x , the gap reopens with inverted band ordering. In recent Angle Resolved Photoemission Spectroscopy (ARPES) experiments, surface states with an odd number of crossings (five surface states crossings) between $\bar{\Gamma}$ and \bar{M} at the Fermi energy

have been observed in this material with $x = 0.1$ [10]. The pure PbTe has inverted bands at the band gap extrema with respect to SnTe. In $\text{Pb}_{1-x}\text{Sn}_x\text{Te}$, initially increasing the concentration of Sn leads to a decreasing band gap. At around $x = 0.35$ (at Helium temperature), the bands cross and the gap reopens for $x > 0.35$ with even parity L^+ band and odd parity L^- band being inverted with respect to each other [15]. The band inversion between PbTe and SnTe results in the existence of helical *interface* states [16–18], which according to Volkov and Pankratov can be described by a 2D mass-less Dirac equation, i.e. the Weyl equation [19].

In this Letter we investigate the optical selection rules governing the low energy excitation of electron-hole pairs around a Dirac point in a 3D TI. Note that the selection rules obtained here are different from the selection rules in ARPES experiments, which record the number of photoelectrons as a function of kinetic energy and emission angle with respect to the sample surface. A number of experiments have shown the existence of the helical surface states in 3D TI [5, 14]. However, a clear understanding of helical surface/interface states in terms of solutions of the Dirac equation is still lacking. Here we show that the helical states in 3D TI naturally emerge from the solutions of the 3D Dirac equation in the presence of a band inversion. As an example, we consider the alloy $\text{Pb}_{1-x}\text{Sn}_x\text{Te}$, which has topologically nontrivial interface states under appropriate doping level. Our results are valid for all strong 3D TIs. $\text{Pb}_{1-x}\text{Sn}_x\text{Te}$ has a rocksalt type crystal lattice with four non-equivalent L points located in the center of the hexagonal facets on [111] axis. The valence and conduction band edges are derived from the hybridized p-type orbitals at the L point [20]. Its end species have inverted band character, L^+ character of PbTe band switches to L^- character of SnTe band and vice versa as shown in Fig. 1. We choose the z -axis to point in direction of the gradient of the concentration ∇x . At the two band extrema, the low energy Hamiltonian is described by a 3D

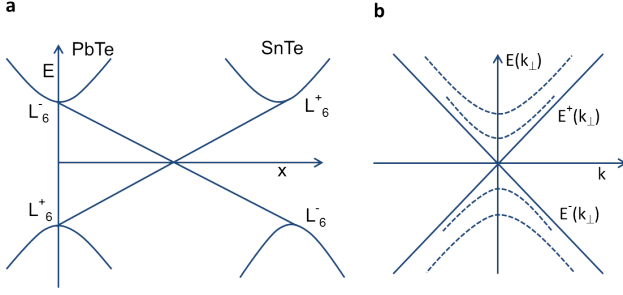


Figure 1: **a**, Band inversion in between two end members in $\text{Pb}_{1-x}\text{Sn}_x\text{Te}$. **b**, Energy spectrum of the inverted contact. The solid lines are Weyl states and dashed lines are additional branches appear for contact thickness $l > l_o$. At the band edges, dispersion is highly linear.

relativistic Dirac equation whose solutions are localized near the $z = 0$ plane where the band crossing occurs, which defines the interface. Dispersion is nearly linear owing to the large band velocities of $v_{\perp} = 8 \times 10^5$ m/s and $v_{\parallel} = 2.24 \times 10^5$ m/s with a small gap [19]. Such peculiar properties at the interface result in a small localization length l_o of the wave function of interface states along the z -axis. Due to the absence of a center of inversion, a Rashba-type spin-orbit coupling is present, which is automatically taken into account in the framework of the Dirac equation. We also present the details of our ab-initio calculation of the bandstructures of these materials in the supercell Brillouin zone obtained by doubling the lattice parameters in each direction. Analysis of the alloy band structures is usually complicated due to folding of the bands from neighboring Brillouin zones, making it difficult to map the calculated bandstructures onto the bandstructures obtained from momentum-resolving experiments. The analysis is further complicated by the presence of impurity bands inside the normal bulk energy gap. The interface states sometimes overlap with bulk energy states. Therefore, we unfold the band structures along the [111] direction in order to shift the band crossing from the Γ point, as seen in the supercell Brillouin zone, to the L point in the primitive cell Brillouin zone [21, 22].

The energy spectrum of $\text{Pb}_{1-x}\text{Sn}_x\text{Te}$ near the L_6^{\mp} band crossing is described by a Dirac Hamiltonian. Within the envelope function approximation, neglecting the far band terms, the interface is described by the two-band Hamiltonian

$$H = \begin{pmatrix} \Delta(z) & \sigma \cdot \hat{\mathbf{p}} \\ \sigma \cdot \hat{\mathbf{p}} & -\Delta(z) \end{pmatrix} \quad (1)$$

where σ are the Pauli matrices, $\hat{\mathbf{p}}$ is the momentum operator with projections $-i\hbar v_{\perp} \nabla_{\perp}$ and $-i\hbar v_{\parallel} \nabla_{\parallel}$ on the xy -plane and along the z axis, respectively, $\Delta(z) = \varepsilon_g(z)/2$ is the gap energy parameter that varies along the z -

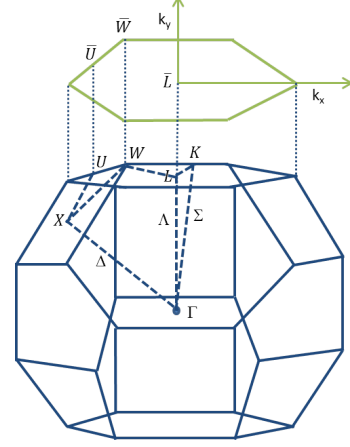


Figure 2: Brillouin zone for rocksalt type crystal with space group $\text{Fm}\bar{3}\text{m}$. There are four inequivalent L points at the center of the faces on the surface of the Brillouin zone. The growth direction is along [111] and is chosen to point along the z -axis. With the appropriate level of doping by Sn atoms in PbTe, band gap goes to zero at L point with a linear excitation energy that traces out a cone in the 2D Fermi surface parallel to the face of Brillouin zone that is perpendicular to the growth direction.

axis. Note that $\Delta(z)$ breaks the translational invariance of the crystal in the z direction and has a symmetry $\Delta(z) = -\Delta(-z)$. The inhomogeneous structure is synthesized by changing the composition along one of the [111] axes, which can be chosen along the z direction. After a unitary transformation of the Hamiltonian, the time-independent Dirac equation can be written as

$$\begin{pmatrix} 0 & i\Delta(z) + \sigma \cdot \hat{\mathbf{p}} \\ -i\Delta(z) + \sigma \cdot \hat{\mathbf{p}} & 0 \end{pmatrix} \begin{pmatrix} \chi_- \\ \chi_+ \end{pmatrix} = (\varepsilon - \varphi(z)) \begin{pmatrix} \chi_- \\ \chi_+ \end{pmatrix} \quad (2)$$

where χ_{\mp} are the two component spinors. The potential $\varphi(z)$ (work function) describes the variation of the gap center. For simplicity we consider the case $\varphi(z) = 0$. From equation (2), the two component spinor χ_{\pm} satisfies

$$(p^2 + u_{\pm}(z, \sigma_z) - \varepsilon^2) \chi_{\pm} = 0 \quad (3)$$

where $u_{\pm}(z, \sigma_z) = \Delta^2 \pm \hbar v_{\parallel} \sigma_z \frac{\partial \Delta}{\partial z}$. In its origin, the linear Weyl spectrum $\varepsilon_o^{\pm}(k_{\perp}) = \pm \hbar v_{\perp} k_{\perp}$ at $k_{\perp} = 0$ is approximately equal to the soliton spectrum in the 1D Peierl's insulator. This implies that $\Delta(z)$ can be chosen to be $\Delta(z) = \Delta(\infty) \tanh(z/l)$. Interface states are localized along the z -axis with the localization length $l_o = \hbar v_{\perp} / \Delta(\infty)$. For $l_o < l$, additional branches with finite mass appear. There are several solutions at $\varepsilon^2 > \Delta^2(\infty)$ which are localized at the contact. For $l_o > l$, only Weyl solutions exist. We focus on the case

when $l_o > l$. Then we have only zero-energy solutions, which correspond to the Weyl states and are given by [19]

$$\Psi'_\pm = C \begin{pmatrix} \pm e^{-\frac{i\theta}{2}} \\ 0 \\ 0 \\ e^{\frac{i\theta}{2}} \end{pmatrix} e \left\{ -\frac{1}{\hbar v_\parallel} \int_0^z \Delta(z') dz' + i\mathbf{k}_\perp \cdot \mathbf{r} \right\} \quad (4)$$

where C is a normalization constant, $\mathbf{k}_\perp = (k_x, k_y, 0)$ and $e^{\mp i\theta} = \frac{k_x \mp ik_y}{k_\perp}$. These solutions have eigenenergies $\varepsilon_o^\pm(k_\perp) = \pm \hbar v_\perp k_\perp$. For $\Delta(z)$ to vanish at the inverted contact, it can be seen from Equation (4) that χ_+ and χ_- must have only non-zero spin down and spin up components, respectively. Each spinor is a mix of spin states from the L^- and L^+ bands. Each spinor at L^\mp band can be represented with the spin up states from the L^- band and spin down states from the L^+ band for both the positive and the negative energies. The motion of the particle at the inverted contact is separated into free motion in (p_x, p_y) and confinement in p_z . A remarkable property of equation (2) is the presence of the zero mode (Weyl mode) localized around $z = 0$. It is this mode that has a locked spin structure. In order to understand the direction in which the 4-spinors point, we have to transform the solutions back to the original basis of the Hamiltonian in Equation (1). With the transformation $\Psi_\pm = U\Psi'_\pm$ where U is the unitary matrix used for the basis transformation, the Weyl solutions are

$$\Psi_\pm = C \begin{pmatrix} \pm e^{-i\frac{(\theta \pm \pi/2)}{2}} \\ \pm e^{i\frac{(\theta \pm \pi/2)}{2}} \\ e^{-i\frac{(\theta \mp \pi/2)}{2}} \\ e^{i\frac{(\theta \mp \pi/2)}{2}} \end{pmatrix} e \left\{ -\frac{1}{\hbar v_\parallel} \int_0^z \Delta(z') dz' + i\mathbf{k}_\perp \cdot \mathbf{r} \right\} \quad (5)$$

where the global phase factors of $e^{\pm i\frac{\pi}{4}}$ are ignored. As a matter of fact, the solutions are helical. In the representation $\Psi_\pm = \begin{pmatrix} \psi_\pm^{L^-} \\ \psi_\pm^{L^+} \end{pmatrix}$, the two spinors $\psi_\pm^{L^-}$ and $\psi_\pm^{L^+}$ refer to the L^- band and L^+ band respectively. It is important to note that the solutions for each sign of the energy are mixed helical states from both bands.

In this representation, the spin directions reveal themselves clearly: Defining $F(\mathbf{r})$ as the position-dependent part, the spins of the 2-spinors $\psi_\pm^{L^-} = \begin{pmatrix} \pm e^{-i\frac{(\theta \pm \pi/2)}{2}} \\ \pm e^{i\frac{(\theta \pm \pi/2)}{2}} \end{pmatrix} F(\mathbf{r})$ and $\psi_\pm^{L^+} = \begin{pmatrix} e^{-i\frac{(\theta \mp \pi/2)}{2}} \\ e^{i\frac{(\theta \mp \pi/2)}{2}} \end{pmatrix} F(\mathbf{r})$ point perpendicular to \mathbf{k}_\perp owing to the $\mp\pi/2$ shifts. This important property will be emphasized with the definition of a new helicity operator for 3D TI later in this Letter. For the states corresponding to the positive eigenvalue at both bands L^\mp , the directions of the spin vectors

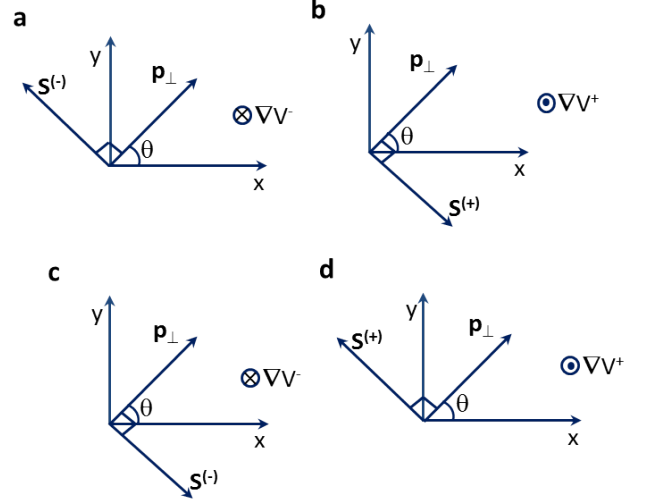


Figure 3: Effect of Rashba spin-orbit coupling. Spin vector $\mathbf{S}^{(-)}$ in the L^- band and spin vector $\mathbf{S}^{(+)}$ in the L^+ band are perpendicular to both the z -axis and \mathbf{p}_\perp . Orientations of the up spin component and down spin component are in opposite directions to each other. **a** and **b** are for the electron with energy, $\varepsilon^+ = +\hbar v_\perp k_\perp$ and **c** and **d** are for the hole with negative energy, $\varepsilon^- = -\hbar v_\perp k_\perp$.

$\mathbf{S}^{(\mp)}$, where the signs \mp refer to the L^\mp bands, associated with the two component spinors point oppositely to each other. For an asymmetric scalar potential V applied to a semiconductor heterostructure, the inversion symmetry is broken, which leads to the Rashba spin-orbit coupling [9, 23]. Here in the case of the interface of a 3D TI we have an asymmetric potential $V^\mp = \pm\Delta$, whose sign depends on the band L^\mp . This results in a band-dependent Rashba spin-orbit coupling. For the positive solution (electrons) the Rashba spin-orbit coupling has the form $H_R = -\lambda_R \boldsymbol{\sigma} \cdot (\mathbf{p} \times \nabla V^\mp) = -\lambda_R \nabla V^\mp \cdot (\boldsymbol{\sigma} \times \mathbf{p}) = \mp \lambda_R \nabla \Delta \cdot (\boldsymbol{\sigma} \times \mathbf{p}) = \mp \lambda_R \frac{\partial \Delta}{\partial z} (\sigma_x p_y - \sigma_y p_x)$, where $\lambda_R \geq 0$ is the Rashba spin-orbit coupling constant. Similarly, for the negative solution (holes), the Rashba spin-orbit coupling is given by $H_R = \lambda_R \boldsymbol{\sigma} \cdot (\mathbf{p} \times \nabla V^\mp) = \pm \lambda_R \frac{\partial \Delta}{\partial z} (\sigma_x p_y - \sigma_y p_x)$. In both cases each spin $\mathbf{S}^{(\mp)}$ is perpendicular both to the momentum and to the potential gradient direction, i.e. the z -axis (see Fig. 3). Our analytical findings are consistent with the spin density functional calculation (DFT) done by Zhao et al. [24].

In a strong TI the surface Fermi circle encloses an odd number of Kramers degenerate Dirac points. The simplest case is a single Dirac point. The surface electronic structure of a 3D TI is similar to a graphene but here we have a single Dirac point rather than having four Dirac points (2 valley \times 2 spin) [7]. In order to determine the Kramers partners explicitly, we rotate the phase of each of the two component spinors by an angle π in the 2D interface plane (see Fig. 4). This rotation yields the

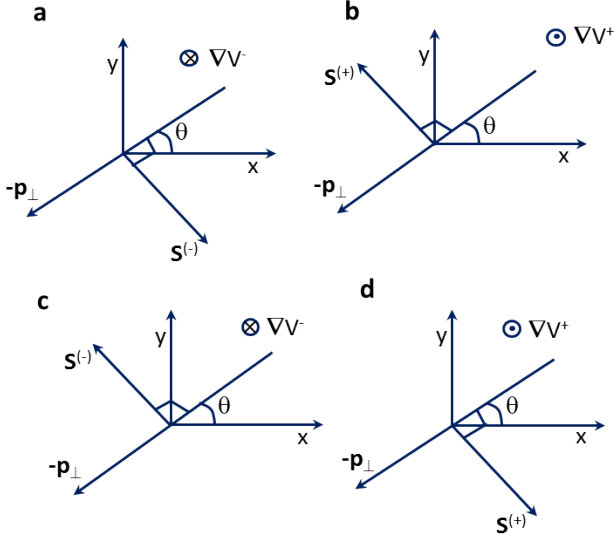


Figure 4: Kramers partners obtained by a π rotation of each two component spinor. Spin direction and momentum direction of each partner are flipped with respect to the spin direction and momentum direction of their respective partners in original basis. **a** and **b** are for positive eigen value and **c** and **d** are for negative eigen value.

$$\text{Kramers partners } \psi_{\pm}^{L^-}(\theta + \pi) = \begin{pmatrix} -e^{-i(\frac{\theta \pm \pi}{2})} \\ -e^{i(\frac{\theta \mp \pi}{2})} \end{pmatrix} F(\mathbf{r})$$

$$\text{and } \psi_{\pm}^{L^+}(\theta + \pi) = \begin{pmatrix} \pm e^{-i(\frac{\theta \pm \pi}{2})} \\ \pm e^{i(\frac{\theta \pm \pi}{2})} \end{pmatrix} F(\mathbf{r}), \text{ where global}$$

phase factors of $e^{\pm i\frac{\pi}{4}}$ have been ignored. Both the spin and momentum direction of each partner component is flipped by an angle π (Fig. 4). This provides a theoretical hallmark of the existence of Kramers partners in 3D TI.

The relevant quantity to characterize the eigenfunctions is their helicity defined as the projection of the momentum operator defined along the spin direction. Helical properties of solutions given by equation (5) are completely general to the 3D TI. Our analytical results show that the spins point in perpendicular direction to the momentum. In the case of free neutrinos in 3D space, the standard helicity operator $\hat{h}_n = -(1/|p_{\perp}|) \boldsymbol{\sigma} \cdot \mathbf{p}$ for the spin $\mathbf{S} = \hbar \boldsymbol{\sigma}/2$ can be used. Similarly, in the case of graphene the helicity for the pseudospin is given by $\hat{h}_g = -(1/|p_{\perp}|) \boldsymbol{\sigma} \cdot \mathbf{p}$. However, in the case of 3D TI this definition is not useful, because the spin points perpendicular to the momentum. Therefore, since we know that the Rashba spin-orbit coupling is responsible for the helicity in 3D TIs, we define the 3D TI helicity operator as $\hat{h}_{\text{TI}} = -(1/|p_{\perp}|) (\boldsymbol{\sigma}_{\perp} \times \mathbf{p}_{\perp}) \cdot \hat{\mathbf{z}}$, where $\boldsymbol{\sigma}_{\perp} = \{\sigma_x, \sigma_y\}$ is the two dimensional vector of Pauli matrices in the xy -plane. \hat{h}_{TI} commutes with the effective single-band Hamiltonian H for the L^- or L^+ band if the expectation value of the spin along the z -axis is zero, which is

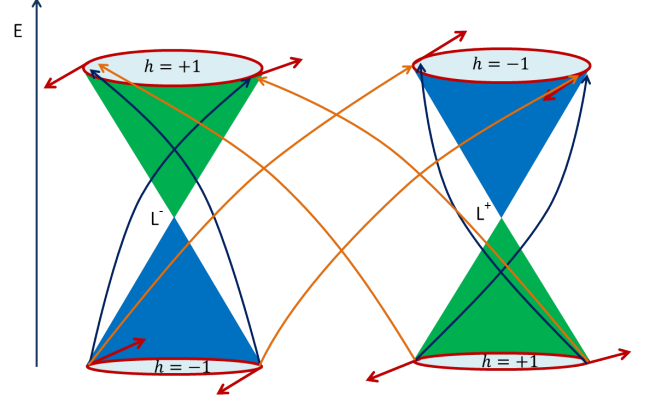


Figure 5: Dirac cones at the crossing between the L^- and L^+ bands. The orange (blue) arrows denote interband (intra-band) transitions. In both types of transitions the spin is conserved. Spins are always tangential to the circle of radius p_{\perp} on the Fermi surface. The color of the cones represents the helicity of the Weyl fermions in the band. In the L^- band the Weyl fermion with positive (negative) energy has positive (negative) helicity, which is denoted by a green (blue) color cone. The helicities are inverted in L^+ band. Note that both cones belong to the same time reversal invariant momentum, in contrast to the K and K' points in graphene. The threshold energy above which an electron-hole pair can be excited is given by the difference in energy between the Dirac point and the Fermi level. The reason for this threshold is the Pauli exclusion principle, which does not allow for double occupation.

valid in our case because the spins lie in the xy -plane. The eigenvalue of the operator \hat{h}_{TI} for the positive energy is $(+1)$ for the L^- band and (-1) for the L^+ band, i.e. $\hat{h}_{\text{TI}} \psi_{\pm}^{L^{\mp}} = (\pm 1) \psi_{\pm}^{L^{\mp}}$. The eigenvalues of \hat{h}_{TI} are reversed in the case of negative energy, i.e. (-1) for the L^- band and $(+1)$ for the L^+ band, $\hat{h}_{\text{TI}} \psi_{\pm}^{L^{\mp}} = (\mp 1) \psi_{\pm}^{L^{\mp}}$ (see Fig. 5).

Now we proceed to calculate the optical selection rules for the excitation of electron-hole pairs, keeping in mind that the Dirac equation provides an effective description of the two-band system consisting of the L^{\mp} bands. It is interesting to compare our results obtained for 3D TI with graphene. Let us represent the four spinors Ψ_{\pm} as a linear combination of the two component spin states from L^{\mp} bands including the periodic part of the Bloch function from each band, $\Psi_{\pm} = \alpha_{\pm} u_{\mathbf{k}}^{L^-} F(\mathbf{r}) + \beta_{\pm} u_{\mathbf{k}}^{L^+} F(\mathbf{r})$, where $\alpha_{\pm} = \begin{pmatrix} \pm e^{-i(\frac{\theta \pm \pi}{2})} \\ \pm e^{i(\frac{\theta \pm \pi}{2})} \end{pmatrix}$ and $\beta_{\pm} = \begin{pmatrix} e^{-i(\frac{\theta \mp \pi}{2})} \\ e^{i(\frac{\theta \mp \pi}{2})} \end{pmatrix}$. The Bloch functions in the two materials on either side of the interface must be similar in order for the effective mass approximation to be valid. An obvious condition is that they must belong to the same point in $\varepsilon_n(\mathbf{k})$. We calculate the low energy transitions around an L valley that is lifted up along the z -direction from the other three L valleys. It is important to note that in the

material we are investigating, with the proper choice of uniform strain, composition and layer width, there exist practically gapless helical states for the [111] valley. In unstrained $\text{Pb}_{1-x}\text{Sn}_x\text{Te}$, band inversion occurs simultaneously at four L points and the phase is topologically trivial. For most experiments, in a structure with interface thickness $d \approx 10$ nm, dispersion of the [111] valley states can be assumed to be gapless while the states in the oblique valleys are gaped [25]. This realization is analogous to the situation in 3D topologically nontrivial materials such as $\text{Be}_2\text{Te}_3/\text{Bi}_2\text{Se}_3$ where the difference in gaps is expected. The helical properties of the localized spin states of 2D Weyl fermions in 3D TI are different from the ones in graphene where the solutions are eigenfunctions of the tight-binding Hamiltonian. Dirac cones at the L^- band and L^+ here resemble the Dirac cones at the K and K' points in graphene; however, both L points in a 3D TI belong to the same k -point in the Brillouin zone. Under the dipole approximation, the transition matrix elements in a 3D TI are given by

$$\begin{aligned} \langle \Psi_+ | \hat{\mathbf{e}} \cdot \mathbf{p} | \Psi_- \rangle = & -4\hbar \sin\left(\frac{\theta' - \theta}{2}\right) \left[-\frac{\hat{\mathbf{e}} \cdot \hat{\mathbf{z}}}{2l_o} + i\hat{\mathbf{e}} \cdot \mathbf{k}_\perp \right] \\ & + 4i\hbar \cos\left(\frac{\theta' - \theta}{2}\right) \sum_{\mathbf{G}} \hat{\mathbf{e}} \cdot \mathbf{G} \text{Im}(a_{L^+}^* a_{L^-}) \quad (6) \end{aligned}$$

where $\hat{\mathbf{e}}$ is the direction of the polarization, \mathbf{G} is the reciprocal lattice vector and a_{L^\pm} are the expansion coefficients of the periodic part of Bloch's functions. The envelope functions are properly normalized. The transition probability can be easily calculated using Fermi's golden rule. Equation (6) has a number of interesting features. When we carefully analyze right hand side of the equation (6), it is evident that the first term corresponds to transitions within the L^- band and within the L^+ band (i.e. intraband) and the second term corresponds to transitions between L^- band and L^+ band (i.e. interband), which are shown in Fig. 5. For the parallel polarizations of light, intraband as well as interband transitions occur simultaneously. The same is true for the perpendicular polarization of light with different strengths of the transition. It is also interesting to note the features associated with equation (6) as a function of polarization angles. On the one hand, for $\theta' - \theta = 0$, transitions are purely interband determined by the crystal symmetry. On the other hand, for $\theta' - \theta = \pi$, transitions are purely intraband with a contribution coming from the envelope function.

The relative weight of the transitions in equation (6) requires a complete calculation of the bandstructures. Therefore, let us calculate the bandstructures and involved dipole matrix elements. Fig. 6 shows our calculations of the complete bulk bandstructures of $\text{Pb}_{1-x}\text{Sn}_x\text{Te}$ at 37.5% doping by Sn impurities in a supercell Brillouin zone using density functional theory within PAW approx-

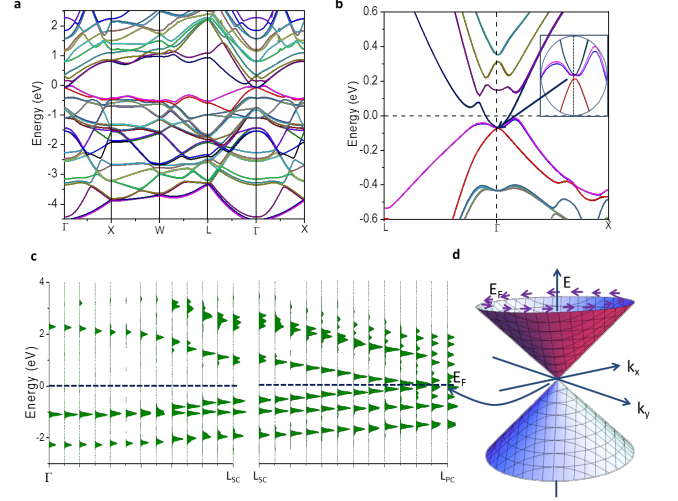


Figure 6: Bulk bandstructure of $\text{Pb}_{1-x}\text{Sn}_x\text{Te}$ at $x = 0.375$ doping level including spin-orbit coupling. In the experiment, the crossing has been reported nearly around $x = 0.35$ at Helium temperature [15]. In the supercell Brillouin zone bands are folded from the neighboring Brillouin zones into the first Brillouin zone (a and b). A minimum band gap of 1.8 meV appears at the Γ point of the supercell Brillouin zone. In fact, the minimum band gap occurs at the L point as in the bandstructures of its parent compounds PbTe and SnTe. This is seen as the bands are unfolded in the primitive cell Brillouin zone, as shown in Figure c, where the bands are unfolded from the Γ to the L point in Δ direction. L_{SC} and L_{PC} are L points in the supercell Brillouin zone and the primitive cell Brillouin zone, respectively. The solid green color in Figure c denote the spectral functions calculated using the recipe described in reference [21]. Bands of opposite parity nearly cross at around 67 meV below the Fermi level at the L point where we observe Dirac cones, Figure c. The unfolded bandstructure facilitates the accurate measurement of the band crossing. A threshold energy of around 67 meV or above is required to excite an electron-hole pair at the L point (d) at 37.5% doping level.

imation as implemented in VASP (Vienna ab initio Simulation Package) [26–28]. We unfold the bandstructures along the Γ point to the L point using the unfolding recipes developed by Popescu and Zunger [21].

There is a small band gap of 1.8 meV at the Γ point. In the unfolded structure the same amount of band gap appears at the L point as in folded structure. This is required by the conservation of energy. In the unfolded structure the bands around the L point are almost linear, which is best described by Weyl fermions. Two bands with opposite parity nearly cross each other at around 67 meV below the Fermi level at the L point. In a recent experiment on Bi_2Se_3 film grown on sapphire, the Dirac point was observed at 135 meV below the Fermi level [29]. In the ARPES measurement for the verification of PbBi_2Te_4 as 3D TI, the Dirac point was observed at 470 meV below the Fermi level [30]. In the unfolded structure, the valence band maximum is derived from the p orbitals

of Pb and Sn hybridized with the s orbital of Te and conduction band minimum is derived from the s orbitals of Pb and Sn hybridized with the p orbital of Te. The valence band maximum and conduction band minimum have opposite parity, thus making interband transitions allowed. The interband dipole matrix elements at 37.5% doping are calculated to be 3.82×10^{-26} Js/m for the perpendicular polarization and 1.12×10^{-25} Js/m for the parallel polarization of the light. The localization length l_o for the Dirac Fermion along z -axis can be obtained using the calculated band gap of 350 meV including spin-orbit coupling for PbTe (Experimental band gap is 190 meV). Using the band velocity, $v_{\parallel} = 2.24 \times 10^5$ m/s, l_o is found to be 0.84 nm. This length measures the characteristic scale of confinement for the Weyl states that exists at the interface.

The dipole matrix elements given by equation (6) are used to calculate the transition probability given by the Fermi's golden rule, shown in Fig. 7. For the parallel polarization of the light, the intraband dipole matrix elements are a little larger than the interband dipole matrix elements, as can be seen in Fig. 7a. For the perpendicular polarization of the light, intraband transitions are dominant, as can be seen in Fig. 7b. For intraband transitions, the transition probability is maximum when the momentum in L^- and in L^+ bands are opposite to each other. 3D polar plots are shown in Figs. 7c and d. They visualize the transitions as a function of polarization angles in $\mathbf{k}_{\perp} = k_o (\hat{x} \cos \theta_{\mathbf{k}} + \hat{y} \sin \theta_{\mathbf{k}})$. The initial and final state have momentum angles $\theta_{\mathbf{k}} = \theta$ and $\theta_{\mathbf{k}} = \theta'$, respectively. For $\theta = 0$ and $\theta' = 0$, transitions are purely interband occurring from L^- to L^+ and vice versa with slightly higher probability in xz -plane. This type of transition is absent in graphene. For $\theta = 0$ and $\theta' = \pi$, transitions are purely intraband occurring only in xz -plane, transitions along y -axis are completely suppressed. This is because the momentum of the initial state is aligned along the x -axis. The transitions occurring along z -axis are governed by the envelope function.

The topological interface states occurring in 3D topologically nontrivial phase are probed using experimental techniques such as ARPES and scanning tunneling microscope [3, 31]. The states are shown to be helical. In this Letter, we show that these states can be derived directly by solving the Dirac equation in 3D. The nature of the helicity of the states is revealed in the solutions. We propose a new helicity operator that identifies the helicity of Weyl fermions in general in all 3D TI. Our theoretical proof of the existence of Kramers partners in 3D TI and helical interface states is very important for the further study of the non-trivial topology of the electronic properties. From our derivations, it has become clear that 2D helical interface states occurring at the interface of 3D TI are different from the helical states occurring in graphene in a number of ways. Most importantly, the optical selection rules proposed for the Weyl fermions in this Letter

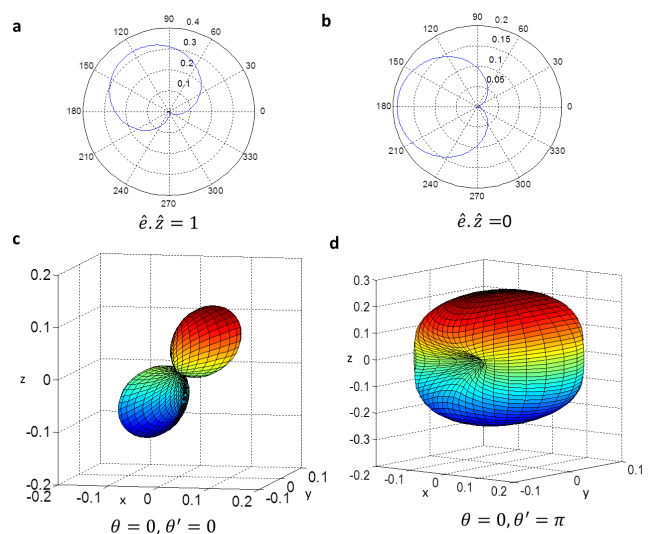


Figure 7: Transition probability calculated using the Fermi's golden rule using the dipole matrix elements given by equation (6). Units are arbitrary. For the incident light polarized parallel to z -axis, both the intraband and interband transitions are significant (a) but the strength of the intraband transitions is higher. For the incident light polarized perpendicular to the z -axis, the transitions are mostly intraband (b). 3D polar plots are shown (c and d) to visualize the transition probability occurring on a sphere as a function of polarization angles. For $\theta = 0$ and $\theta' = 0$, transitions are purely interband and for $\theta = 0$ and $\theta' = \pi$ transitions are purely intraband.

show that the transitions are both intraband and interband at the L point, in contrast to graphene where the transitions are purely intraband (Fig. 5). These selection rules (equation (6)) we found are of great importance for the excitation of electron-hole pairs in low power optoelectronic applications.

We acknowledge support from NSF (Grant ECCS-0901784), AFOSR (Grant FA9550-09-1-0450), and NSF (Grant ECCS-1128597). M.N.L. thanks Daniel Loss for fruitful discussions during his stay at the University of Basel, Switzerland. M.N.L. acknowledges partial support from the Swiss National Science Foundation.

* Electronic address: michael.leuenberger@ucf.edu

- [1] Moore, J. E. The birth of topological insulators. *Nature* **464**, 194 (2010).
- [2] Hasan, M. Z. & Kane C. L. Colloquium: Topological insulators. *Rev. Mod. Phys.* **82**, 3045 (2010).
- [3] Hsieh, D. *et al.* A tunable topological insulator in the spin helical Dirac transport regime. *Nature* **460**, 1101-1106 (2009).
- [4] Hajlaoui, M. *et al.* Ultrafast Surface Carrier Dynamics in the Topological Insulator Bi_2Te_3 . *Nano Lett.* **12**, 3532-3536 (2012).

- [5] Xia, Y. *et al.* Observation of a large-gap topological-insulator class with a single Dirac cone on the surface. *Nature Physics* **5**, 398 (2009).
- [6] Kane, C. L. & Mele, E. J. Z₂ topological order and the quantum spin hall effect. *Phys. Rev. Lett.* **95**, 146802 (2005).
- [7] Fu, L. & Kane, C. L. Topological insulators with inversion symmetry. *Phys. Rev. B* **76**, 045302 (2007).
- [8] Konig, M. *et al.* Quantum spin Hall insulator state in HgTe quantum wells. *Nature Physics* **5**, 438 (2009).
- [9] Bychkov, Y.A. & Rashba, E.I. Properties of a 2D electron gas with lifted spectral degeneracy. *JETP Lett.* **39**, 78 (1984)
- [10] Hsieh, D. *et al.* Topological Dirac insulator in a quantum spin hall phase. *Nature* **452**, 970-974 (2008).
- [11] Kenz, I.; Du, R. R. & Sullivan, G. Evidence for Helical Edge Modes in Inverted InAs/GaSb Quantum Wells. *Phys. Rev. Lett.* **107**, 136603 (2011).
- [12] Moore, J. E. & Balents, L. Topological invariants of time-reversal-invariant band structures. *Phys. Rev. B* **75**, 121306(R) (2007).
- [13] Fu, L., Kane, C. L. & Mele, E. J. Topological insulators in three dimensions. *Phys. Rev. Lett.* **98**, 106803 (2007).
- [14] Chen, Y. L. *et al.* Experimental Realization of a Three-Dimensional Topological Insulator, Bi₂Te₃. *Science* **325**, 178 (2009).
- [15] Dimmock, J. O., Melngailis, I. & Strauss, A. J. Band structure and laser action in Pb_xSn_{1-x}Te. *Phys. Rev. Lett.* **16**, 1193 (1966).
- [16] Pankratov, O. A. Electronic properties of band-inverted heterojunctions: supersymmetry in narrow-gap semiconductors. *Semicond. Sci. Technol.* **5**, S204-S209 (1990).
- [17] Korenman, V. & Drew H. D. Subbands in the gap in inverted-band semiconductor quantum wells. *Phys. Rev. B* **35**, 6446 (1987).
- [18] Agassi, D. & Korenman, V. Interface states in band-inverted semiconductor heterojunctions. *Phys. Rev. B* **37**, 10095 (1987).
- [19] Volkov, B. A. & Pankratov. Two-dimensional massless electrons in an inverted contact. *JETP Lett.* **42**, 178 (1985).
- [20] Gao, X. & Daw, M. S. Investigation of band inversion in (Pb,Sn)Te using ab initio calculations. *Phys. Rev. B* **77**, 033103 (2008).
- [21] Popescu, V. & Zunger, A. Extracting E versus k effective band structure from supercell calculations on alloys and impurities. *Phys. Rev. B* **85**, 085201 (2012).
- [22] Ku, W., Berlijn, T. & Lee, C. Unfolding first-principles band structures. *Phys. Rev. Lett.* **104**, 216401 (2010).
- [23] e Silva, de A., Rocca, G. C. L. & Bassani, F. Spin-orbit splitting of electronic states in semiconductor asymmetric quantum wells. *Phys. Rev. B* **55**, 16293 (1997).
- [24] Zhao, Y. *et al.* Helical States of Topological Insulator Bi₂Se₃. *Nano lett.* **11**, 2088-2091 (2011).
- [25] Buczko, R., Cywinski. L., PbTe/PbSnTe heterstructures as analogs of topological insulators. Preprint <http://arxiv.org/abs/1202.2315>.
- [26] Kresse, G.; Furthmuller, J. Efficient iterative schemes for ab initio total-energy calculations using a plane-wave basis set. *Phys. Rev. B* **54**, 11169 (1996).
- [27] Kresse, G.; Hafner, J. Norm-conserving and ultrasoft pseudopotentials for first-row and transition elements. *J. Phys.: Condens. Matter* **6**, 8245 (1994).
- [28] Blochl, P.E. Projector augmented-wave method. *Phys. Rev. B* **50**, 17953 (1994).
- [29] Chang, C. Z. Growth of Quantum Well Films of Topological Insulator Bi₂Se₃ on Insulating Substrate. Preprint <http://arxiv.org/abs/1012.5716>.
- [30] Kuroda, K. *et al.* Experimental Verification of PbBi₂Te₄ as a 3D Topological Insulator. *Phys. Rev. Lett.* **108**, 206803 (2012).
- [31] Zhang, H., *et al.* Topological insulators in Bi₂Se₃, Bi₂Te₃ and Sb₂Te₃ with a single Dirac cone on the surface. *Nature Physics* **5**, 438 (2009).